Int J Adv Manuf Technol (2012) 59:1037–1045
DOI 10.1007/s00170-011-3571-4

ORIGINAL ARTICLE

Multiphysics simulation of laser–material interaction during laser powder depositon

Felipe Vásquez · Jorge Andres Ramos-Grez · Magdalena Walczak

Received: 19 April 2011 / Accepted: 3 August 2011 / Published online: 26 August 2011

Abstract This work reports a theoretical and numerical study of the parameters related to the process of laser powder deposition through a lateral nozzle. For this purpose, a 3D quasi-stationary finite element model was developed analytically and implemented numerically. The proposed model estimates the shape of the melt pool depending on the process parameters including scanning speed, powder mass flow, laser power, and physical properties. Also, phase transformations and physical properties (density, thermal conductivity, and specific heat) vary as function of temperature. In addition, thermo-capillary forces and their effect on fluid flow inside the melt pool are considered. The obtained set of equations coupled through the temperature variable was solved using COMSOL Multiphysics. The results are presented and compared with previously obtained experimental data, in which chromium powder was deposited, allowing validation of the model. Finally, variations at the melt pool geometry in terms of the operational parameters are analyzed. This model aims at estimation of melt pool geometry during laser powder deposition in time reasonably short to allow for predictable process control.

Keywords Laser powder deposition · Melt pool geometry · Multiphysics simulation · Laser–material interaction

F. Vásquez · J. A. Ramos-Grez (✉) · M. Walczak
Department of Mechanical and Metallurgical Engineering,
School of Engineering, Pontificia Universidad Católica de Chile,
Av. Vicuña Mackenna 4860,
Macul, Santiago, Chile
e-mail: jramos@ing.puc.cl

1 Introduction

The metal processing industry, in its continuing quest to improve products and reduce costs, requires parts with special surface properties, such as good resistance to corrosion and wear, to be produced reliably within certain constrains. Unlike conventional methods, the laser cladding process is accurate, fast, and provides better bonding between materials and smaller heat-affected zones offering potential advantages for the processing industry.

Among the different laser powder deposition processes, one finds laser cladding as one of the most promising options. Compared with conventional machining process used for 3D shaping of mechanical parts, it can reduce considerably the amount of material wasted due to chip formation [1]. The laser cladding process is defined as the process in which laser beam is used to fuse a material which has different metallurgical properties than the substrate, whereby only a very thin layer of the substrate has to be melted in order to achieve metallurgical bonding with minimal dilution of added material and substrate so that the original properties of the coating material are maintained [2]. In practice, laser cladding makes possible to solve problems such as wear of diesel engine exhaust valves [3], wear of tools made of high speed steel [4], reparation of mold steels [5], corrosion of gas turbine blades [6], and other problems that would be impossible solving using conventional methods, like heat treatment [7].

During the past 25 years, the number of studies devoted to welding, alloying, and plating using laser beam as a heat source has been increasing considerably, the primary motivation being a better understanding and control of the process as required for manufacturing and remanufacturing of mechanical parts. Modeling and simulation of these laser processes can help improving process

prediction and system control in a direct and reliable manner. One of the first models published in literature was one consisting of a 2D model solving transient equation for convection diffusion of matter in the melt pool examined for laser alloying [8]. This research revealed that the injected powder particles melt instantly when arriving to the pool and that the average solute contents increases linearly with increasing interaction time. Interactions between the powder particles, the laser beam, and the molten pool were taken into account in the first 3D model allowing the computation of the melt pool shape [9]. Incorporation of convection within the melt pool helped explaining some features of the resulting microstructure [10]. The development of numerical methods in the last two decades has motivated further improvements of the models, including time distribution of the laser energy during cladding and its effect on melt pool geometry [11]. Interactions between laser, substrate, and powder as well as powder–substrate interactions have also been implemented [12]. In general, due to the physical complexity of the involved physical phenomena, the early models were simplified by ignoring some of the phenomena, e.g., heat convection [13], melting of the substrate material [14], radiation losses from the liquid pool [15, 16], or fluid flow in the liquid pool [17], which did not allow for accurate prediction of the shape of melt pool. In particular, the nonconsideration of the phenomena occurring at the liquid/gas interface should not be omitted as Marangoni flow induced by surface tension gradients, which is known to be largely responsible for the broadening of the top of the melt pool [18, 19]. The first models incorporating the effect considered a modified thermal conductivity to account for thermo-capillary phenomena of the liquid metal without calculating the fluid flow [20–22]. Later, transient models including the entire thermo-capillary problem were developed as shown for single- [23], double-track coaxial [24], and multilayered off-axial cladding [25]. However, an accurate model accounting for all the important phenomena cannot be solved analytically and numerical approaches are still computationally intensive.

In the present work, laser–substrate interaction during laser powder deposition is simulated by a multiphysics model with special emphasis on the evolution of melt pool geometry during the process. The model is verified on a previous experimental work [26] in which chromium powder was applied on AISI/SAE 1020 steel plates. The multiphysics approach allows for simultaneous solution of multiple phenomena by coupling through a common variable, in this case, temperature. The purpose of the model is to diminish the experimental effort in predicting the geometry and properties of the cladded surface as required by metal processing industry [27]. The last is made possible by solving the model in a reasonably short time.

The model considers the most important aspects of the melt pool formation, i.e., conservation of momentum, conservation of mass, and conservation of energy. In addition, phase transformations, dependence of physical properties on actual temperature, Marangoni effect of the liquid phase, and the flux of vapor at the liquid/gas interface are included. Finally, it is examined how the operational parameters such as laser power, laser scanning speed, and powder mass flow affect the geometry of the resulting melt pool.

2 Model development

The setup used in the previously realized experiment [27] consisted in a lateral nozzle providing chromium powder at 45º angle from the z axis (Fig. 1). The laser source used for the process was a CO_2 laser with a maximum power of 3.5 kW and a wavelength of 10.6 μm. The powder used for deposition was chromium with an average particle size of 34 μm (atomized). Details of the setup are explained elsewhere [27].

The developed computational model is based on the terms of laser power that enters and exits from the molten pool, considering the process to be pseudo-stationary and allowing for surface vaporization along with the effects of phase transformations (solid–liquid and liquid–vapor).

2.1 Domain and boundary conditions

Two domains have been generated, both referring to the base material (Fig. 2), but the solid–liquid phase transformations are only allowed in Domain 2.

2.1.1 Domain conditions

Domain 1 In this domain, the energy equation for heat conduction in solid is solved quasi-stationary (Eq. 1):

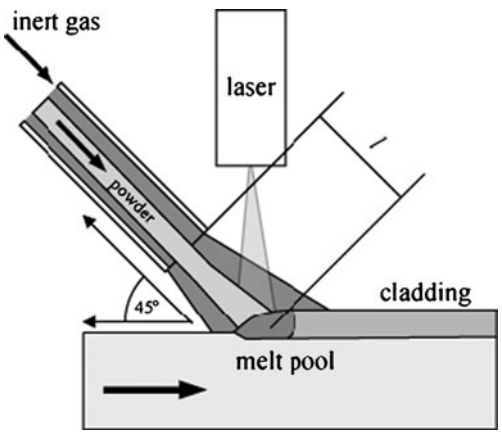

Fig. 1 Experimental setup with lateral nozzle

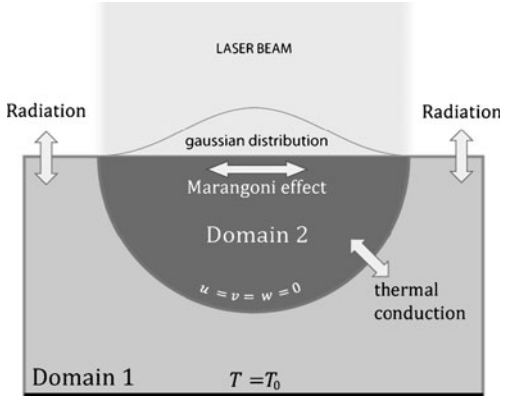

Fig. 2 Geometric configuration of the domains and boundary conditions

(1) Conservation of energy:

$$\rho C_{\mathrm{p}}^{\mathrm{eq}}(\nabla T) - \nabla \cdot (k \nabla T) = Q \tag{1}$$

Where ρ, $C_{\mathrm{p}}^{\mathrm{eq}}$, k, and T are density, equivalent specific heat, thermal conductivity, and temperature, respectively.

Domain 2 In this domain, in addition to the energy equation (Eq. 1), conservation of momentum (Eq. 4) and conservation of mass (Eq. 6) are solved. The last two equations are modified to include the variation of physical properties in the function of temperature, the effect of phase transformations, surface evaporation, and Marangoni effect, as follows:

For the conservation of energy, the equivalent specific heat which takes into account the latent heat of fusion L_{f} (Eq. 2), where f_{L} is the liquid fraction, assumed to vary linearly with temperature (Eq. 3) [28]:

$$C_{\mathrm{p}}^{\mathrm{eq}} = C_{\mathrm{p}} + L_{\mathrm{f}} f_{\mathrm{L}} / (T_{\mathrm{m}} - T_0) \tag{2}$$

$$f_{\mathrm{L}} = \begin{cases} 1 & , \quad T > T_{\mathrm{L}} \\ \dfrac{T - T_{\mathrm{S}}}{T_{\mathrm{L}} - T_{\mathrm{S}}} & , \quad T_{\mathrm{S}} \le T \le T_{\mathrm{L}} \\ 0 & , \quad T < T_{\mathrm{L}} \end{cases} \tag{3}$$

where T_{S} and T_{L} are the liquidus and solidus temperatures, respectively.

(2) Conservation of momentum:

Conservation of momentum given by (Eq. 4) includes buoyancy force in the melt pool given by (Eq. 5) [29]:

$$\rho(U \cdot \nabla U) = F_{\mathrm{V}} - \nabla p + \mu \nabla \cdot (\nabla U) \tag{4}$$

$$F_{\mathrm{V}} = \rho_{\mathrm{S}}(1 - \beta(T - T_{\mathrm{L}}))g \tag{5}$$

where ρ_{S}, β, T_{m}, μ, and U are density of the substrate when solid, thermal expansion coefficient, substrate melting temperature, dynamic viscosity, and vector of fluid velocity, respectively.

(3) Conservation of mass:

$$\nabla U = 0 \tag{6}$$

In addition, physical properties, density ρ, heat capacity C_{p}, and thermal conductivity k are considered functions of temperature (Eqs. 7, 8, 9, and 10) [12]:

$$\rho = \rho_{\mathrm{S}}(1 - g_{\mathrm{L}}) + \rho_{\mathrm{L}} g_{\mathrm{L}} \tag{7}$$

$$C_{\mathrm{p}} = C_{\mathrm{pS}}(1 - f_{\mathrm{L}}) + C_{\mathrm{pL}} f_{\mathrm{L}} \tag{8}$$

$$k = k_{\mathrm{S}}(1 - g_{\mathrm{L}}) + k_{\mathrm{L}} g_{\mathrm{L}} \tag{9}$$

$$f_{\mathrm{L}} = \frac{g_{\mathrm{L}} \rho_{\mathrm{L}}}{\rho}, \quad f_{\mathrm{L}} + f_{\mathrm{S}} = 1, \quad g_{\mathrm{L}} + g_{\mathrm{S}} = 1 \tag{10}$$

where g_{s}, g_{L}, f_{S}, f_{L}, C_{pS}, C_{pL}, k_{S}, and k_{L} are volume fraction of solid, volume fraction of liquid, mass fraction of solid, mass fraction of liquid, specific heat of solid, specific heat of liquid, thermal conductivity of solid, and thermal conductivity of liquid, respectively.

2.1.2 Boundary conditions

The boundary conditions are represented schematically in Fig. 2.

Base material at the surface and sides These surfaces are considered to irradiate the absorbed energy to the air, without convection (Eq. 11). Convection is considered negligible because the time scale of heat input by the laser is much shorter than convective heat losses due to relatively fast scanning velocity [30]:

$$-k \frac{\partial T}{\partial z} = \sigma \varepsilon \left(T^4 - T_0^4\right) \tag{11}$$

where σ, ε, T_0, are the Stefan–Boltzmann constant, surface emissivity of the base material, and room temperature, respectively.

Surface interacting with the laser beam Apart from the energy irradiation change in surface tension due to

Marangoni effect (Eqs. 12, 13, and 14) is taken into account:

$$\mu\frac{\partial u}{\partial z} = -\frac{\partial \gamma}{\partial T}\frac{\partial T}{\partial x} \tag{12}$$

$$\mu\frac{\partial v}{\partial z} = -\frac{\partial \gamma}{\partial T}\frac{\partial T}{\partial y} \tag{13}$$

$$w = 0 \tag{14}$$

Where u, v, w, and $\partial\gamma/\partial T$ are the components of the fluid flow velocity and change of surface tension with respect to temperature (assumed to be negative and constant [12]), respectively.

Bottom of the base material Due to support by a massive steel plate, the bottom of the base material maintains its initial temperature (Eq. 15) throughout the experiment:

$$T = T_0 \tag{15}$$

Hemisphere surface This artificial border demarcates the domain in which phase transformations (solid–liquid and liquid–gas) are allowed, from the domain in which solid state is maintained with the condition described by Eq. 16:

$$u = v = w = 0 \tag{16}$$

2.1.3 Quantity of vapor mass escaping from the pool

The amount of vapor that escapes from the pool is calculated by considering the analytical form of Stefan's condition under a quasi-steady state (Eq. 17) [31]:

$$AI + k_1\frac{\partial T}{\partial z} = \rho_1 \dot{S}_v L_v \tag{17}$$

where $\dot{S}_v$ and L_v are velocity of the liquid–vapor interface and latent heat of boiling, respectively. The quantity of vapor mass m_{ev} that escapes from the pool surface is obtained using Eq. 18:

$$m_{ev} = \dot{S}_v \rho r_1^2 \pi\tau \tag{18}$$

2.1.4 Simulation details

The model has been implemented in COMSOL Multiphysics 4.0 and solved in 3D using a stationary iterative solver (GMRES) for Eqs. 1, 4, and 8 coupled by the variable of temperature. The solution time was of 691.8 s for 59,946 degrees of freedom of 35,373 tetrahedral mesh elements as obtained on a regular PC (3 GHz Intel Core Duo, 4 GB RAM). The simulation was adjusted by the parameter δ that weighs the attenuated power. The value of δ was determined to be 0.3 for all experiments, as it minimizes the error between the experimental and calculated values of melt pool depth, z_{max} (Fig. 3).

The values of all parameters used in the model are listed in Table 1.

2.2 Simplifications

Although the presented model includes all the important features of the problem, several simplifications and assumptions were introduced:

- Laser radiation of fixed power P_w is distributed over a circular beam with constant radius r_1 centered on the z axis and it moves along the x direction. It is assumed that the beam power has a Gaussian power distribution (TEM_{00}), which allows the distribution of laser power density I on the metal surface to be described by Eq. (20):

$$I = \frac{2}{\pi r_1^2} P_w e^{-\frac{2}{r_1^2}\sqrt{x^2+y^2+z^2}} \tag{20}$$

  where r_1, P_w, x, y, and z are radius of the laser beam, initial laser power, and the spatial coordinates, respectively.
- The powder particles are considered to be identical spheres of radius r_p.
- All powder particles are transferred at a uniform velocity V_p at the distance l from the source to the interaction plane between laser light and the base

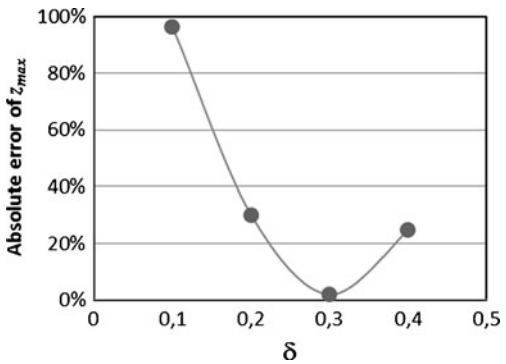

Fig. 3 Absolute error of calculated melt pool depth (z_{max}) in the function of the parameter δ

Table 1 Parameters and constants used in the numerical simulation

Parameter/constant	Symbol	Value	Reference
Powder mass flow	$\dot{m}$	2.5 g/min	–
Laser scanning speed	U	2 mm/s	–
Laser beam radius	r_l	0.25 mm	–
Melting temperature	T_m	1,811 K	[33]
Boling temperature	T_v	3,135 K	[34]
Ambient temperature	T_0	293 K	–
Latent heat of fusion	L_f	$247{\cdot}10^3$ J/(kg)	[35]
Latent heat of vaporization	L_v	$6.25{\cdot}10^5$ J/kg	[36]
Specific heat, solid	C_{pS}	502 J/(kg·K)	[31]
Specific heat, liquid	C_{pL}	620 J/(kg·K)	[35]
Specific heat, vapor	C_{pv}	747.14 J/(kg·K)	[31]
Density, liquid	ρ_l	6350 kg/m^3	[28]
Density, solid	ρ_s	7500 kg/m^3	[28]
Liquid-state thermal conductivity	k_l	43 W/(m·K)	[37]
Solid-state thermal conductivity	k_s	40 W/(m·K)	–
Dynamic viscosity	μ	$5{\cdot}10^{-3}$ kg/m/s	[33]
Coefficient of thermal expansion	β	$1.45{\cdot}10^{-4}$ 1/K	[37]
Variation of surface tension with temperature	$\partial\gamma/\partial T$	$-5{\cdot}10^{-4}$ N/m/K	[33]
Velocity of powder particles	V_p	26 m/s	–
Travel distance of powder	l	25 mm	–
Average radius of powder particles	r_p	34 μm	–
Nozzle diameter	d	1.8 mm	–
Density of powder particles	ρ_c	7.19 g/cm^3	[38]

material. Collisions between particles are neglected, thus laser attenuation P_{att} by the powder particles can be described by Eq. (21):

$$P_{att} = P_\omega \delta \left[1 - \exp\left(-\frac{3Q_{ext}\dot{m}l}{\pi r_p D_P^2 \rho_c V_P}\right)\right] \quad (21)$$

Where δ, Q_{ext}, $\dot{m}$, D_p, and ρ_c are fitting parameter, extintion coefficient, mass flow rate, area covered by powder cloud, and density of the powder, respectively.

- The melt pool width w_{max} is equal to the diameter of the laser beam at the illuminated surface. The melt pool is considered having a semi-circular cross-section, which is consistent with the geometry obtained experimentally.
- Energy absorptions by the base material and by the powder particles remain constant during the entire process.
- There is no heat loss by convection or radiation from particles in the stream flow due to the short time of interaction with the laser light.
- The amount of energy absorbed by the powder particles is less than 2% of the amount of energy reaching the surface of the base material (determined based on experimental observation [26]).

3 Results and discussion

In the previous work [26], several experiments of laser powder deposition were realized. These experiments were carried out using chromium powder as clad material and AISI/SAE 1020 steel as substrate. The experiments were performed with a fixed focal length, laser power ranging from 300 to 500 W, and with powder mass flow between 0.05 and 5.5 g/min. Argon gas was used to minimize oxidation of the treated surface.

Results from these experiments were used to validate the computational model described in Section 2. In order to facilitate the comparison, the experimentally obtained geometries were normalized by the laser beam average radius of 0.25 mm.

3.1 Comparison between simulation and experimental results

Correlation between the geometry of the melt pool obtained experimentally and computationally is shown in Figs. 4 and 5. Both width and depth of fusion reveal a good correlation with $R^2>0.95$ with a slight underestimation of z_{max} (slope< 1) and slight overestimation of w_{max} (slope>1). The comparison of the results for different laser powers was

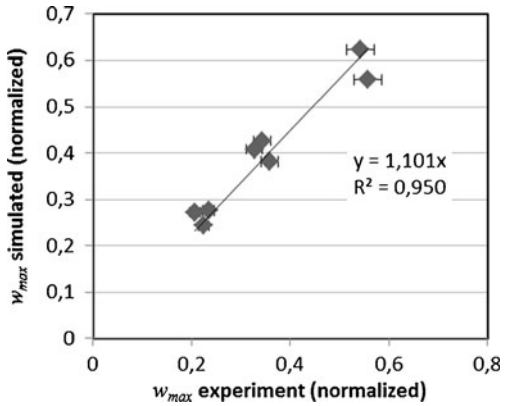

Fig. 4 Fusion width (w_{max}): comparison between simulation and experiment

obtained for constant laser scanning speed of 2 mm/s and mass flow of 2.5 g/min as shown in Fig. 6. Figure 7 shows the cross-section area of fusion zone (for w_{max}) in terms of power for different input levels of powder mass flow: 0.05, 2.5, and 5.5 g/min.

3.2 Effect of operational parameters on the melt pool geometry

In order to determine which laser power, powder mass flow, and scanning speed are more suitable for laser powder deposition, it is necessary to understand how these parameters affect the resulting geometry of the melt pool. The following results were obtained using the computational model.

3.2.1 Effect of powder mass flow

When applying higher amount of powder, the pool depth decreases (Fig. 8), which can be explained by more energy

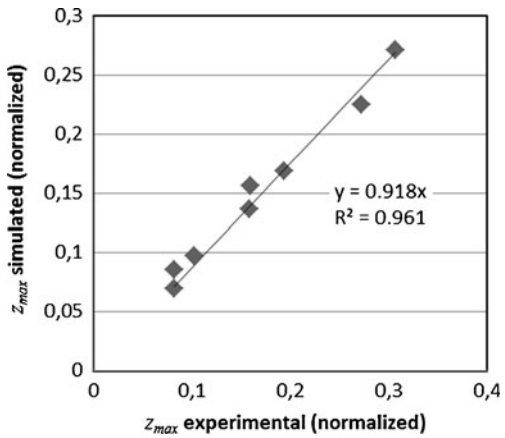

Fig. 5 Fusion depth (z_{max}): comparison between simulation and experiment

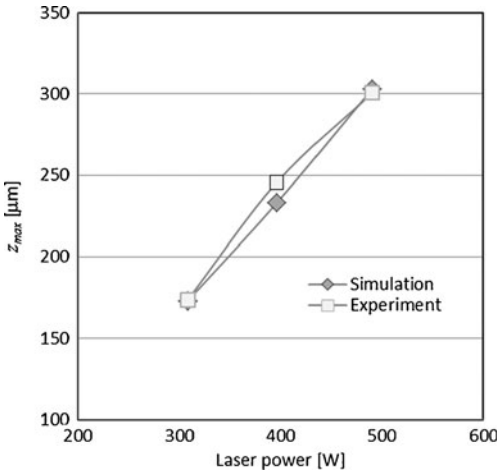

Fig. 6 Fusion depth vs. laser power obtained for the mass flow of 2.5 g/min and scanning speed of 2 mm/s

being reflected by the particles interacting with the laser beam. Numerical results show that there is a 49% decrease in the depth of the melt pool when the mass flow is 10 g/min compared with the absence of particles as revealed for laser power of 600 W and laser scanning speed of 2 mm/s. The relationship between laser power and depth of the melt pool is consistent with the prediction made by Rosenthal [32]. It should be noted that the model does not consider the energy intake from the heated powder particles arriving to the metal surface.

3.2.2 Effect of laser scanning speed

By increasing the speed of laser scanning, the melt pool depth decreases (Fig. 9), which can be expected because a

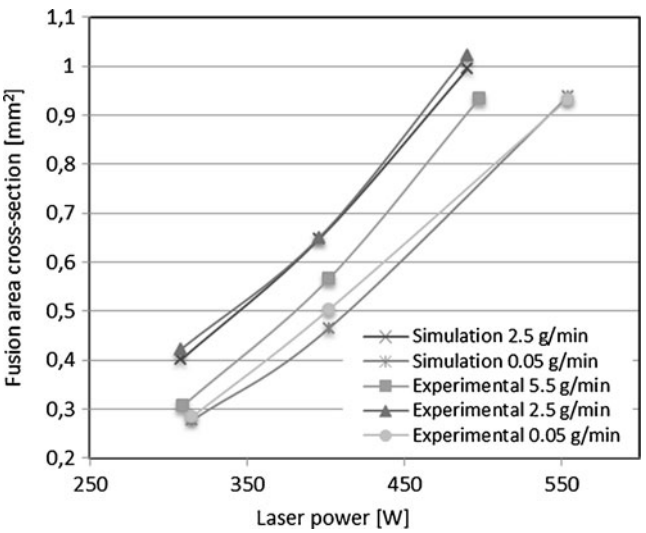

Fig. 7 Fusion area cross-section as function of laser power for different mass flows

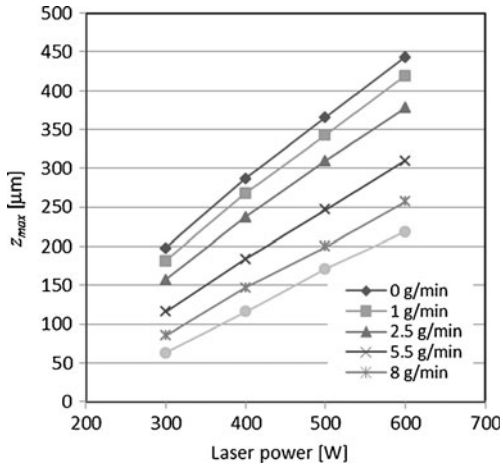

Fig. 8 Variation of fusion depth with laser power for different mass flows and a fixed laser scanning speed of 2 mm/s

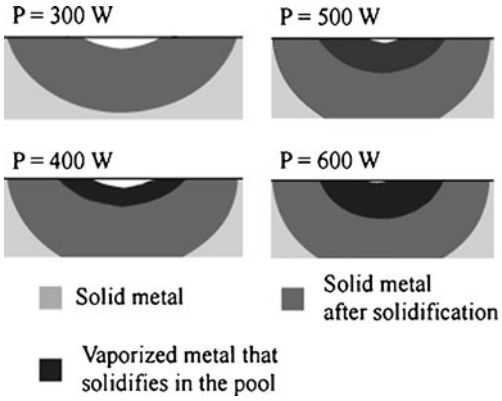

Fig. 10 Geometry of the melt pool obtained by simulation. Metal vapor trapped by plasma and solidified after cooling is considered. Laser scanning speed of 2 mm/s and mass flow of 2.5 g/min

shorter interaction time of the laser beam with the material surface results in a lower overall temperature in the pool. The variation of this parameter has a lesser effect on depth of melt than an increase of powder mass flow, obtaining a decrease of 22% when comparing the extreme cases of stationary beam (0 mm/s) and the scanning speed of 20 mm/s (laser power 600 W, mass flow 2.5 g/min).

3.2.3 Metal evaporation

Our simulation indicates that as laser power increases, the amount of vapor leaving the pool's outer surface decreases. This effect is explained by the pressure exerted on the surface of the base material by the plasma, which increases with laser power. This result is consistent with the literature data [31].

The vapor trapped by the plasma is returned to the solid phase after cooling of the melt pool as shown in Fig. 10. With a laser power of 300 W, all the vaporized metal escapes from the pool; whereas at a higher power, the increased pressure exerted by the plasma prevents the output of vapor from the pool. With a laser power of 600 W, 94% of the metal solidifies in the pool. It can be seen that a greater amount of vapor escapes from the center of the pool decreasing towards the sides. This can be explained by the Gaussian distribution of the laser beam energy, considering homogenous distribution of the pressure exerted by the plasma.

Figure 11 shows the total vaporized mass, vaporized mass that escapes from the pool (Eq. 20), and the vaporized mass that escapes from the pool obtained by COMSOL modeling. The difference between the results obtained by the analytical solution of the Stefan's equation and the results obtained by COMSOL take place below 400 W. This strong discrepancy is due to the different way the effect of plasma pressure is incorporated in the respective models.

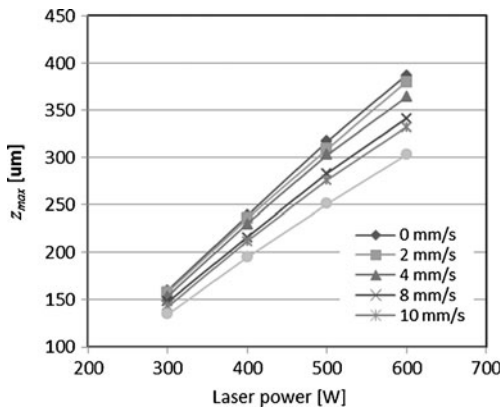

Fig. 9 Variation of fusion depth with laser power for different laser scanning speeds and a fixed mass flow of 2.5 g/min

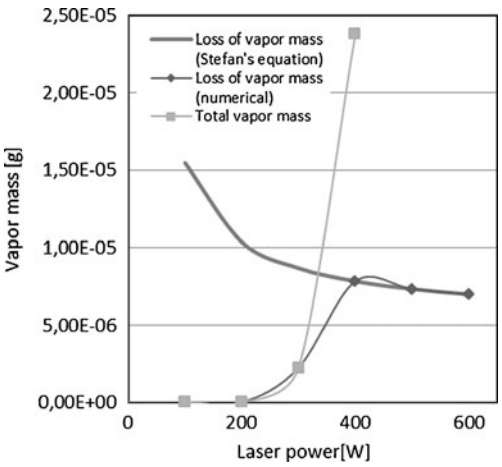

Fig. 11 Comparison of the mass loss due the vaporization obtained for the interaction time τ=0.25 s, laser scanning speed of 2 mm/s, and mass flow of 2.5 g/min

3.2.4 Effect of surface tension

Figures 12 and 13 show how the geometry of the resultant clad varies depending on the laser power. The higher the power of the laser, the more vigorous is the movement of the liquid metal. Due to temperature gradient, the fluid is forced to move away from areas where surface tension is lower. In our case the surface tension is lower at the center of the pool, which results in a concave shape of the illuminated surface.

4 Conclusions

It was possible to develop and implement a computational model with a high degree of agreement with the experimental results obtained in a previous work. This model includes the most relevant physical phenomena that take place in the process of laser powder deposition and provides results within 12 min on a regular PC. It was possible to study how the resulting clad geometry is affected by the most important parameters: laser power, mass flow, and laser scanning speed.

A continuous model was used to solve the equations of mass, momentum, and energy conservation including nonlinear equations at the laser interaction area, which allowed the inclusion of phase transformations. The attenuation of the laser beam due to energy absorption by powder particles was also considered.

This model helps in understanding how the changes in laser power, mass flow, and scanning speed affect size and shape of the melt pool.

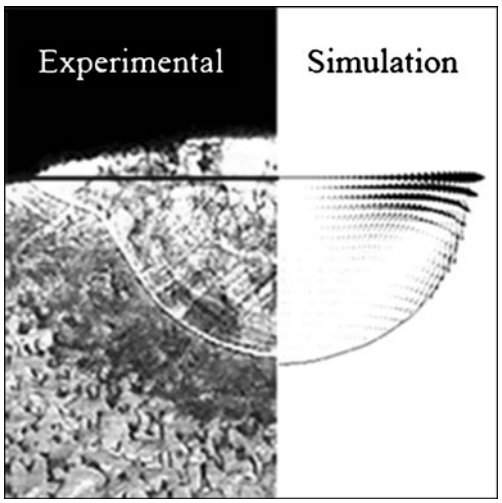

Fig. 12 Movement of the liquid phase produced by gradient of surface tension obtained by simulation (*right*) and the geometry obtained experimentally (*left*) for a laser power of 308 W, mass flow of 2.5 g/min, and scanning speed 2 mm/s

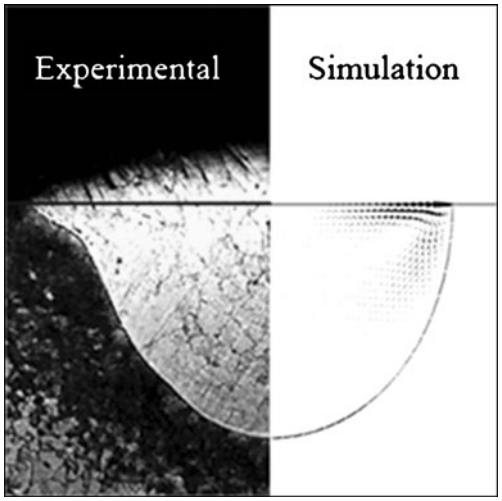

Fig. 13 Movement of the liquid phase produced by gradient of surface tension obtained by simulation (*right*) and the geometry obtained experimentally (*left*) for a laser power of 490 W, mass flow of 2.5 g/min, and scanning speed of 2 mm/s

It can be concluded that the effects produced by operational parameters on the geometry of the melt pool are:

- Laser power: The applied power is the most relevant factor in the laser cladding process. By increasing laser power, both depth (z_{max}) and width (w_{max}) of the fusion zone increase. By changing laser power from 300 to 600 W, the depth of fusion increases by the factor of 2.4, while the width increases by the factor of 1.76.

  Further, there are indirect effects of laser power:

  – Material loss by evaporation: An increase in laser power decreases the output of vapor from the pool, which is explained by the increasing pressure of plasma on the laser affected area. As a result, at high laser power evaporation is minimized.
  – Surface tension: The surface tension has an important effect on the melt pool geometry as it determines its final shape. The effect is explained by the liquid metal moving from areas of lower surface tension to areas of higher surface tension.

- Mass flow: By increasing the amount of powder used for cladding, the depth of the melt pool and the area of molten material decrease, which is associated with scattering of laser light at the powder particles. The model predicts a linear dependence between the depth of melting and the power applied, regardless the amount of deposited powder.
- Laser scanning speed: This parameter strongly influences the cross-sectional dimensions of the melt pool. By increasing the speed of laser scanning, the melt pool depth decreases.

Acknowledgment The authors would like to thank Ambrosio Olivos for the skillful sample fabrication and preliminary analyses. This work has been supported by the Chilean Council of Research and Technology, CONICYT (FONDECYT Project No.11090183).

References

1. Taberner I, Lamikiz A, Ukar E, López de Lacalle LN, Angulo C, Urbikain G (2010) Numerical simulation and experimental validation of powder flux. J Mater Proces Technol 210:2125–2134
2. Komvopoulos K (1990) Processing and characterization of laser-cladded coating materials. J Eng Mater Technol 112:131–143
3. Navas C, Conde A, Cadenas M, de Damborenea J (2006) Tribological properties of laser clad Stellite 6 coatings on steel substrates. Surf Eng 22:26–34
4. Darmawan W, Quesada J, Rossi F, Marchal R, Machi F, Usuki H (2009) Improvement in wear characteristics of the AISI M2 by laser cladding and melting. J Laser Appl 21:176–182
5. Navas C, Conde A, Fernandez BJ, Zubiri F, de Damborenea J (2005) Laser coatings to improve wear resistance of mould steel. Surf Coat Technol 194:136–142
6. Wang HY, Zuo DW, Chen G, Sun GF, Li XF, Cheng X (2010) Hot corrosion behaviour of low Al NiCoCrAlY cladded coatings reinforced by nano-particles on a Ni-base super alloy. Corros Sci 52:3561–3567
7. Zhong M, Liu W (2010) Laser surface cladding: the state of the art and challenges. Proc IMechE C—J Mech Eng Sci 224:1041–1060
8. Chande T, Mazumder J (1985) Two dimensional, transient model for mass transport in laser surface alloying. J Appl Phys 57 (6):2226–2232
9. Picasso M, Marsden CF, Wgniere JD, Frend A, Rappaz M (1994) A simple but realistic model for laser cladding. Metall Mater Trans B—Proc Metall Mater Proce Sci 25(2):281–291
10. Picasso M, Hoadley A (1994) Finite element simulation of laser surface treatments including convection in the melt pool. Int J Num Meth Heat & Fluid Flow 4(1):61–83
11. Toyserkani E, Khajepour A, Corbin S (2004) 3-D finite element modeling of laser cladding by powder injection: effects of laser pulse shaping on the process. Optics Lasers Eng 41(6):849–867
12. Han L, Phatak KM, Liou F (2004) Modeling of laser cladding with powder injection. Metall Mater Trans B 35B:1139–1150
13. Kar A, Mazumder (1987) One-dimensional diffusion model for extended solid solution in laser cladding. J Appl Phys 61:2645–2655
14. Hoadley AFA, Rappaz M (1992) A thermal model of laser cladding by powder injection. Metall Trans B 23(5):631–642
15. Pinkerton AJ, Li L (2004) Modelling the geometry of a moving laser melt pool and deposition track via energy and mass balances. J Phys D 37:1885–1895
16. Pinkerton AJ, Li L (2004) An analytical model of energy distribution in laser direct metal deposition. Proc Inst Mech Eng Part B 218:363–374
17. Cho C, Zhao G, Kwak S-Y, Kim SB (2004) Computational mechanics of laser cladding process. J Mater Process Technol 153–154:494–500
18. Zacharia T, David SA, Vitek JM, Debroy T (1989) Weld pool development during GTA and laser-beam welding of type 304 stainless steel. 1. Theoretical analysis. Weld J 68(12):S499–S509
19. Lampa C, Powell J, Ivarson A, Magnusson C (1995) Factors affecting the efficiency of laser welding. Lasers Eng 4(1):73–83
20. Lampa C, Kaplan AFH, Powell J, Magnusson C (1997) An analytical thermodynamic model of laser welding. J Phys D Appl Phys 30(9):1293–1299
21. Toyserkani E, Khajepour A, Corbin S (2003) Three-dimensional finite element modeling of laser cladding by powder injection: effects of powder feedrate and travel speed on the process. J Laser Appl 15(3):153–160
22. Fathi A, Toyserkani E, Khajepour A, Durali M (2006) Prediction of melt pool depth and dilution in laser powder deposition. J Phys D Appl Phys 39(12):2613–2623
23. He X, Mazumder J (2007) Transport phenomena during direct metal deposition. J Appl Phys 101(5):053113
24. He X, Yu G, Mazumder J (2010) Temperature and composition profile during double-track laser cladding of H13 tool steel. J Phys D Appl Phys 43(1):015502
25. Kong F, Kovacevic R (2010) Modeling of heat transfer and fluid flow in the laser multilayered cladding process. Metall Mater Trans B 41(6):1310–1320
26. Olivos A, Ramos-Grez J, Walczak M (2011) Surface hardness of mild steel (AISI/SAE 1020) after laser surface alloying with Chromium. Lasers Eng (in press)
27. Lalas C, Tsirbas K, Salonitis K, Chryssolouris G (2007) An analytical model of the laser clad geometry. Int J Adv Manuf Technol 32:34–41
28. Traidia A, Roger F, Guyotv E (2010) Optimal parameters for pulsed gas tungsten arc welding in partially and fully penetrated weld pools. Int J Therm Sci 49(7):1197–1208
29. Kou S (1986) Three-dimensional convection in laser melted pools. Metall Trans A 17A:1986–2265
30. Pinkerton AJ, Li L (2004) An analytical model of energy distribution in laser direct metal deposition. Proc I Mech E Part B J Eng Manuf 218:363–74
31. Sankaranarayanan S, Kar A (1999) Nonlinear effects of laser–plasma interaction on melt-surface temperature. J Phys D Appl Phys 32:777–784
32. Rosenthal D (1946) The theory of moving sources of heat and its application to metal. Trans ASME 68:849–866
33. Robert A, Debroy T (2001) Geometry of laser spot welds from dimensionless numbers. Metall Mater Trans 32B:941–947
34. Debroy T, Basu S, Mundra K (1991) Probing laser induced metal vaporization by gas dynamics and liquid pool transport phenomena. J Appl Phys 70(3):1313–1319
35. Islam D (2000) Laser cutters. Central Michigan University, Michigan
36. Pinkerton A, Li L (2004) Modelling the geometry of a moving laser melt pool and deposition track via energy and mass balances. J Phys D Appl Phys 37:1885–1895
37. Qi H, Mazumder J (2006) Numerical simulation of heat transfer and fluid flow in coaxial laser. J Appl Phys 100:024903
38. Davis, JR (ed.) (1998) Metals handbook, 2nd ed. ASM International, Metals Park, Ohio